Self-organized biotectonics of termite nests

Alexander Heyde[a], Lijie Guo[b], Christian Jost[b], Guy Theraulaz[b], and L. Mahadevan[a,c,d,1]

[a]Department of Organismic and Evolutionary Biology, Harvard University, Cambridge, MA 02138; [b]Centre de Recherches sur la Cognition Animale, Centre de Biologie Intégrative, Université de Toulouse, CNRS, Université de Toulouse–Paul Sabatier, 31062 Toulouse France; [c]School of Engineering and Applied Sciences, Harvard University, Cambridge, MA 02138; and [d]Department of Physics, Harvard University, Cambridge, MA 02138

Edited by Simon A. Levin, Princeton University, Princeton, NJ, and approved November 16, 2020 (received for review April 16, 2020)

The termite nest is one of the architectural wonders of the living world, built by the collective action of workers in a colony. Each nest has several characteristic structural motifs that allow for efficient ventilation, cooling, and traversal. We use tomography to quantify the nest architecture of the African termite *Apicotermes lamani*, consisting of regularly spaced floors connected by scattered linear and helicoidal ramps. To understand how these elaborate structures are built and arranged, we formulate a minimal model for the spatiotemporal evolution of three hydrodynamic fields—mud, termites, and pheromones—linking environmental physics to collective building behavior using simple local rules based on experimental observations. We find that floors and ramps emerge as solutions of the governing equations, with statistics consistent with observations of *A. lamani* nests. Our study demonstrates how a local self-reinforcing biotectonic scheme is capable of generating an architecture that is simultaneously adaptable and functional, and likely to be relevant for a range of other animal-built structures.

collective animal behavior | termite nests | stigmergy | ecophysiology | morphogenesis

Termite nests are among the most complex and impressive structures produced by animal societies (1–3) and serve to create a microniche that allows for the controllable exchange of matter and energy with the environment (4–6). Even when compared with the many animal species that exhibit collective behaviors, including coordinated motion, active synchronization, or shared decision making (7, 8), the collective activities of social insects such as the highly eusocial termite are exceptional, in that they often lead to the formation of intricate physical structures: shelters (9); trail networks (10); and, most prominently, nests (1, 2). These structures are not merely the byproduct of animal behavior, however, since they also play a central role in regulating the flow of information necessary for their own construction and function. Nest building in social insects is thus considered an exemplar of functional self-organization, and studying this process can inform us about how structure and function emerge in ecophysiology (11).

The eusocial termites of the genus *Apicotermes* typify the architectural complexity that can be produced by social insects. These termites, native to the savannahs and forests of Africa, construct small ovoid nests just 20 to 40 cm in diameter, located 5 to 50 cm underground (12). The nest structure must be efficiently constructed to be capable of passive ventilation and cooling (4–6, 13–15), while remaining habitable and traversable by the termites within. This is no small feat—given the scale and complexity of *Apicotermes* nests, it is not feasible that any single termite has a sufficiently broad cognitive map of the organization of the whole structure to coordinate the actions of the colony (16). Yet even in the absence of centralized control, these nests clearly show coherent structure at a global scale, pointing to the collective self-organization of several thousand termites acting only on their local conditions to produce global order (3, 11, 16).

Rather than termites sharing information by direct communication (such as via antennal contact or gestures), Grassé (17) proposed that termite workers communicate indirectly by coupling their building actions with the deposition of a local stimulus (such as a secreted building pheromone) in nearby substrate. This principle of stigmergy—defined as the spontaneous but indirect coordination of agents stimulated to action by the trace of previous actions left in the environment (16)—has already been implicated in the morphogenesis of the large structures that enclose the nest. Over the long length and time scales of the overall mound structure, the small internal tunnels and chambers within the mound influence the mound material porosity (2, 15); mediate ventilation (5, 6); and suffice to explain the coarse features of the mound, such as its shape, size, and temporal evolution (18).

However, this leaves open questions of how the internal structural motifs are formed and maintained at shorter length scales in the mound microstructure. These questions have only recently begun to be addressed in other insects, like in the far simpler structures of the ant *Lasius niger* (19), typically with computationally expensive individual-based modeling rather than continuum approaches. Overall, the comparatively more complex architecture of *Apicotermes* nests begs two important questions: First, what are the structural motifs within the nest, and how are they arranged? And second, how are they formed via the dynamic feedback loop between individual behavior and emerging structure in the nest construction process?

Digitization and Structure of *Apicotermes* Nests

To answer these questions, we first collected, scanned, and statistically analyzed the structure of nests in the species *Apicotermes lamani*. Two nests (MeMo14, Fig. 1*A*, and MeMo13, Fig. 1*B*)

Significance

Termite nests are a remarkable example of functional self-organization that show how structure and function emerge on multiple length and time scales in ecophysiology. To understand the process by which this arises, we document the labyrinthine architecture within the subterranean nests of the African termite *Apicotermes lamani* and develop a simple mathematical model that relies on the physical and biological interactions between termites, pheromones, and mud in the nest. Our model explains the formation of parallel floors connected by linear and helical ramps, consistent with observations of real nests. In describing this multiagent system, we elucidate principles of physical and behavioral coupling with relevance to swarm intelligence and architectural design.

Author contributions: A.H., G.T., and L.M. designed research; A.H. and L.M. performed research; A.H., L.G., C.J., G.T., and L.M. contributed new reagents/analytic tools; A.H., L.G., C.J., and L.M. analyzed data; and A.H., G.T., and L.M. wrote the paper.

The authors declare no competing interest.

This article is a PNAS Direct Submission.

[1]To whom correspondence may be addressed. Email: lmahadev@g.harvard.edu.

This article contains supporting information online at https://www.pnas.org/lookup/suppl/doi:10.1073/pnas.2006985118/-/DCSupplemental.

Published January 18, 2021.

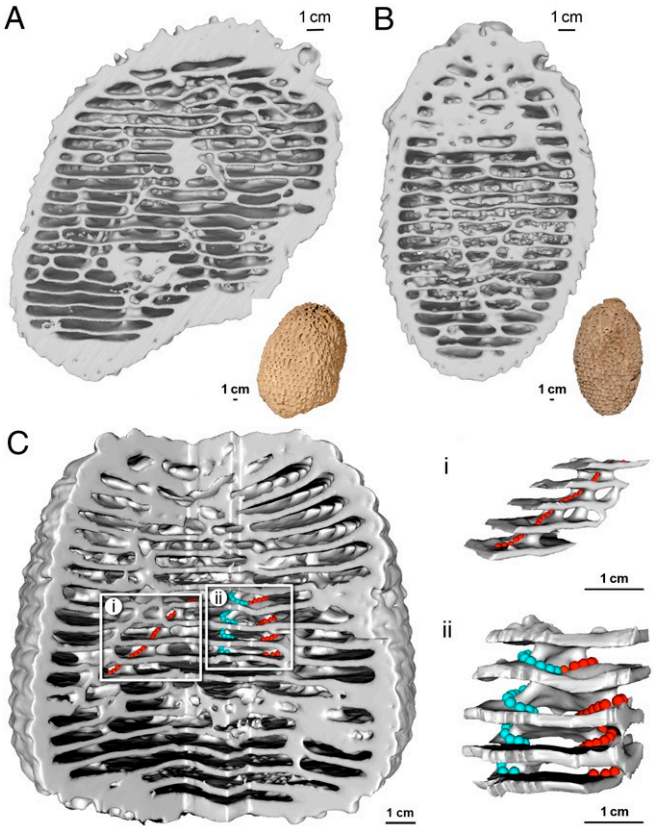

Fig. 1. Digital reconstruction of *A. lamani* nests reveals layered floors and chambers connected by linear and helicoidal ramps. (*A* and *B*) Cutaway view of two *A. lamani* nests, collected around Libreville (Gabon): MeMo14 (*A*) and MeMo13 (*B*). The nests were digitized with X-ray computer tomography and reconstructed in three dimensions (3D). (*C*) A large *A. lamani* nest (*Left*, MeMo80) collected in 2008 near Pointe Noire (Republic of the Congo) with examples of a linear ramp (*C*, *i*, red dots) and two helicoidal ramps with opposing chirality (*C*, *ii*, red and cyan dots).

were collected near Libreville, Gabon (*SI Appendix*, Fig. S1), although one of these (MeMo13) showed too much internal damage for a statistical analysis. A third nest (MeMo80, Fig. 1*C*) was collected in 2008 near Pointe Noire in the Republic of the Congo (*SI Appendix*, Fig. S1); in this nest, we measured that workers had length 4 to 5 mm and height 2 to 3 mm, while soldiers had length 8 to 10 mm with a height of 2 to 3 mm (12) (*SI Appendix*, Table S1). We digitized and imaged the excavated nests with a medical X-ray computed-tomography (CT) scanner (*Materials and Methods*), allowing for nondestructive exploration of the complete three-dimensional internal structure of each nest (Movie S1).

Both nests showed a similar external appearance and, based on our X-ray CT scans, also shared a similar internal architecture consisting of many floor layers arranged in parallel, with several vertical pillars connecting adjacent floors (Fig. 1 *A* and *B*). To investigate these structures, we systematically searched our two digitized examples for open corridors connecting floors (*Materials and Methods*), and we identified several occurrences of two types of ramps (Fig. 1*C*): linear ramps (15 in MeMo80 and 23 in MeMo14), in which a path connects floors along a linear incline, and helicoidal ramps (5 in MeMo80), in which the path spirals around a central pillar as it spans floors. The helicoidal ramps had no clearly preferred chirality (three left, two right), although a pair of co-occurring left-handed and right-handed helicoidal ramps was identified (Fig. 1 *C*, *ii*).

We then examined the internal architecture of the two *A. lamani* nests (MeMo80 and MeMo14; *SI Appendix*, Table S1) for which we had data, to quantify the spacing and arrangement of floors and ramps. For each nest, we assembled a series of 359 and 177 vertical slices, respectively (Fig. 2*A*), and measured the thickness of each floor and the vertical spacing between floors (Fig. 2*B*). In total, our dataset included 35 floors (17 in MeMo80 and 18 in MeMo14), sufficient to conduct separate analyses on each of the two nests. The floor thickness was on average 1.7 mm (median = 1.6 mm) in nest MeMo80 and on average 1.8 mm (median = 1.2 mm) in nest MeMo14. The floor spacing was on average 4.6 mm (median = 4.7 mm) in nest MeMo80 and on average 7.2 mm (median = 7.7 mm) in nest MeMo14. For both nests, the variance in floor thickness was low (coefficient of variation [CV] = 0.31 in MeMo80, CV = 0.59 in MeMo14), as was the variance in floor spacing (CV = 0.19 in MeMo80, CV = 0.22 in MeMo14), demonstrating that the flooring of the termite nests is arranged at regular vertical frequencies, with a strong continuity between adjacent floors (*SI Appendix*, Fig. S1 *B* and *C*).

Given this consistent arrangement of floors, we next investigated the positioning of ramps within the nests by measuring the horizontal distance from each ramp to the nearest ramp on the same floor (Fig. 2*C*). In MeMo80, we found a mean same-floor distance of 27.4 mm (median = 25.4 mm, CV = 0.41), and in MeMo14 this mean distance was 25.7 mm (median = 27.1 mm, CV = 0.33); these both deviated from a null model of randomly scattered ramps (Kolmogorov–Smirnov [KS] test, $P = 0.047$ for MeMo80, $P = 0.022$ for MeMo14; *SI Appendix*). We compared these measurements with the horizontal distance between ramps on adjacent floors. Because these ramps were often directly connected, this distance was much smaller for both nests, with a mean of 12.9 mm (median = 9.2 mm, CV = 0.79) in MeMo80 and a mean of 7.1 mm (median = 6.5 mm, CV = 0.47) in MeMo14, deviating in the opposite direction from the null model (KS test, $P = 0.046$ for MeMo80, $P = 0.040$ for MeMo14). Hence, while ramps tended to be spaced at fairly large, regular intervals across a floor, they tended to be positioned near ramps on adjacent floors, allowing for efficient vertical traversal between nest levels.

A Minimal Model of Biotectonics

To address how these structures are formed, we turn to a series of observations, old and new, to motivate a minimal continuum model of nest construction. With no evidence of design or a designer, termites build in response to local cues such as the nearby mound structure and secreted pheromones (17, 20). The resulting architecture both enables and constrains the movement of pheromones and termites and thereby modifies behavior, so that nest construction can be seen as a result of a feedback loop linking physical and behavioral dynamics (Fig. 3*A*). The architecture of the nest dictates which spaces are accessible to termite workers, the density of termite workers in turn controls the concentration of secreted pheromone, and the information carried by the pheromone profile in turn serves as a template for the ongoing remodeling of the nest architecture, thereby completing the feedback loop of nest morphogenesis.

We therefore model the spatiotemporal dynamics of three fields that depend on location denoted by the vector $\mathbf{x}$ and time t: the nest material density $u(\mathbf{x}, t)$, scaled from no nest material ($u = 0$) to fully compacted ($u = 1$), as well as the termite worker density $n(\mathbf{x}, t)$ and the pheromone concentration $\rho(\mathbf{x}, t)$, both in units of mass per volume. These three fields jointly evolve according to a set of conservation laws, expressed as the following differential equations (*SI Appendix*) for the nest material, termite workers, and pheromone levels:

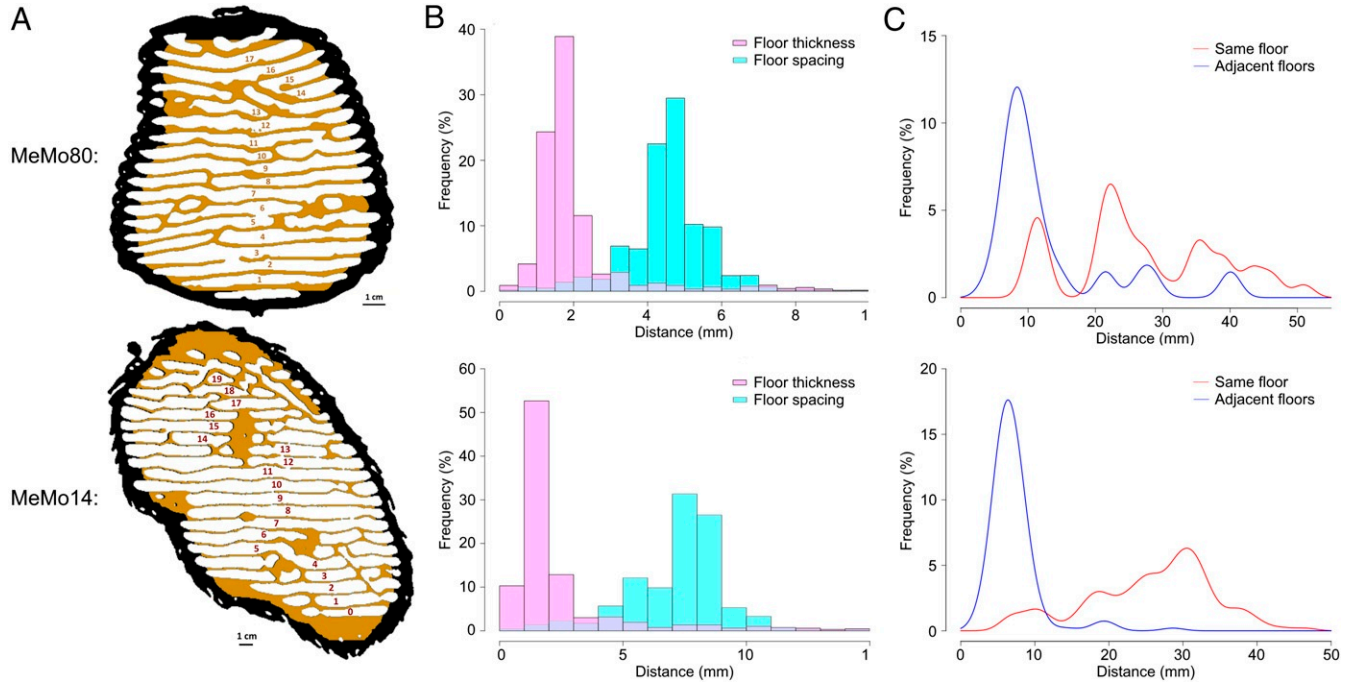

Fig. 2. Statistical analysis of *A. lamani* nests shows consistent floor and ramp spacing. (*A–C*, *Top*) Nest MeMo80. (*A–C*, *Bottom*) Nest MeMo14. (*A*) Representative vertical slices of nest structure with floors labeled in average height order. (*B*) Histograms for floor thickness (pink) and spacing between floors (cyan), measured in millimeters, corresponding to the nest depicted in *A*. Both the thickness of and spacing between floors tend to fall within a consistent band in each nest. (*C*) Density plot for the horizontal distance from a ramp to the nearest other ramp on the same floor (red) or on an adjacent floor above or below (blue), corresponding to the nest depicted in *A*. Ramps on the same floor tend to be spaced out, while ramps on adjacent floors often connect directly, resulting in minimal spacing.

$$\text{Nest material: } \partial_t u = \partial_z\,[g\partial_z u] + f_+ - f_-, \qquad [1]$$

$$\text{Termite workers: } \partial_t n_\pm = \nabla\cdot[(1-u)D\nabla n_\pm + \chi n_\pm \nabla u] \pm (f_- - f_+)k^{-1}, \qquad [2]$$

$$\text{Pheromone: } \partial_t \rho = \nabla\cdot[\delta\nabla\rho] + Hf_+ - \gamma\rho, \qquad [3]$$

where ∂_t and ∂_z are the differential operators in time and height, respectively; $\nabla\cdot$ is the three-dimensional divergence operator; and ∇ is the three-dimensional gradient operator. Here Eq. **1** reflects the addition and removal of the nest material, with f_+ and f_- denoting the building and removal rates of dirt (whose functional form is discussed below). Moreover, the poroelastic diffusivity of dirt g captures its capacity to settle under the influence of gravity (21); this term breaks the rotational symmetry of the model equations and establishes a defined vertical orientation for the nest. Eq. **2** reflects the dynamics of termites carrying dirt n_+ or not carrying dirt n_-, with a flux that has two components: an effective diffusivity that is proportional to the amount of open space, i.e., $(1-u)D$, as well as a chemotactic term that drives termite workers into open and low-density nest regions with chemotactic coefficient χ (22, 23). The final term represents switching between n_+ and n_-, with the pellet size k denoting the average amount of dirt transported by a worker. Finally, Eq. **3** reflects the dynamics of pheromones as they diffuse with a diffusion coefficient δ, are secreted into deposited soil at a level H per pellet (19), and degrade through evaporation at a rate γ. We note that the pheromone is relatively nonvolatile and thus not advected by the ambient fluid, since the subterranean nests of *Apicotermes* do not typically have noticeable temperature gradients (24).

To complete the formulation of our model, we require functional forms for the building rate f_+ and removal rate f_-. Although these rates have not been directly measured in *A. lamani* termites, the building rate has been investigated for the neotropical termite *Procornitermes araujoi* (25), and both rates have also been quantified in the ant *L. niger* (19). In all cases, we find that the local nest density scales directly with the building rate and inversely with the removal rate, resulting in high-density regions becoming increasingly compacted while low-density regions are excavated. Moreover, this positive feedback is mediated by a pheromone added by the workers to the building material (Fig. 3*B*), so that the termites are more likely to deposit dirt in regions marked by pheromone as being sites of active remodeling and so that building does not take place either where there is no nest material ($u=0$) or where the nest material is already fully compacted ($u=1$). It is reasonable also that the removal rate scales with the density of termite workers not carrying dirt and with the density of dirt u available for removal. Given these basic considerations, the simplest possible functional forms for f_+ and f_- are

$$\text{Building rate: } f_+ = r_+ n_+ \rho u(1-u), \qquad [4]$$

$$\text{Removal rate: } f_- = r_- n_- u, \qquad [5]$$

where $r_\pm$ are rate constants. With these choices, the dynamics of nest morphogenesis as described by our model can be captured by only a small number of nondimensional parameters: the scaled pheromone potency Hr_+/r_-; the scaled evaporative flux γ/r_-; the pellet size k; and the scaled diffusivities δ/D, χ/D, and g/D (*SI Appendix*). For simplicity, and to directly study the self-contained organization of this system, we model the nest as a closed three-dimensional domain, using no-flux boundary conditions, such that when integrated over the nest domain the total number of termites $|n|$ and the total quantity of dirt u are conserved. With this formulation, our model describes the simultaneous disassembly and reassembly of the nest, which are features of both initial nest construction and its ongoing renovation during its lifespan (19).

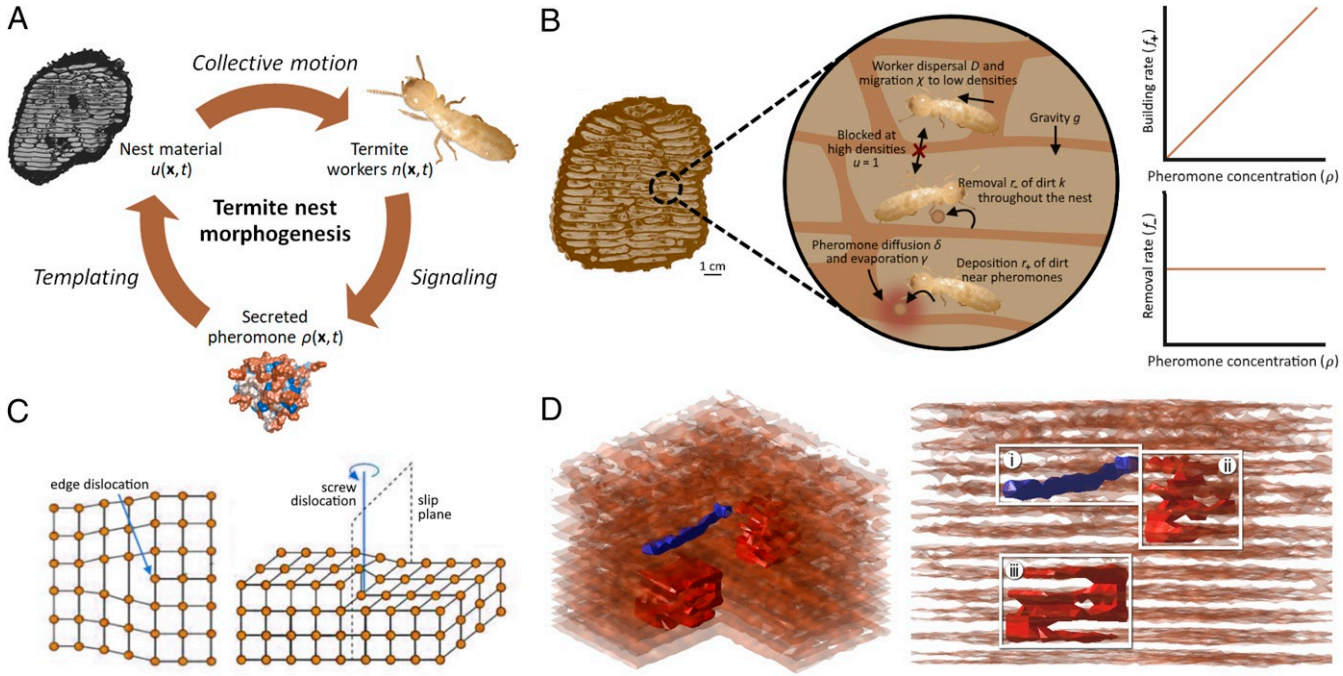

Fig. 3. Biotectonic model predicts floor spacing and ramp emergence in termite nests. (*A*) Model schematic of the feedback loop driving nest construction, highlighting the interactions between nest material *u*, termite workers *n*, and secreted pheromone ρ. (*B*) Illustration of a local region of a nest, showing the processes in our model. Termite workers migrate preferentially to low-density regions and cannot travel through very high-density regions. Workers remove dirt throughout the nest but are more likely to deposit dirt near pheromones which they release during deposition. Pheromones are assumed to have a low diffusivity and hence provide a local signal. (*C*) Diagrams of edge and screw dislocations in floor patterning. Edge dislocations that result from floor misalignment can give rise to linear ramps, while screw dislocations can lead to helicoidal ramps that pivot about a slip plane. (*D*) Three-dimensional reconstruction of a nest simulated according to our construction model, shown here at two angles. This simulated nest contains one linear ramp (*i*, blue) and two helicoidal ramps (*ii* and *iii*, red).

Natural Patterns in Simulated Nests

We conducted 500 independent simulations of nest construction by initializing our model each time with uniform nest density $u(\mathbf{x}, t)$ and pheromone concentration $\rho(\mathbf{x}, t)$, and with a randomly dispersed density of termite workers $n(\mathbf{x}, t)$, using measured and inferred parameter values from several studies on termite nest structure and behavior (*SI Appendix*, Table S2) and a numerical implementation of a stable Euler differencing scheme (*Materials and Methods*) run until a steady-state distribution of floor thickness and separation is achieved. Nest construction time ranged from 25.5 to 94.6 d (95% confidence interval; *SI Appendix*, Fig. S6). The model generated simulated nests (*SI Appendix*, Fig. S3 *A–C*) with regularly spaced floors of roughly planar orientation (orthogonal to the direction of gravity in the model) and a floor thickness that scales as $(\delta/\gamma)^{1/2}$ in some regimes (*Materials and Methods* and *SI Appendix*, Fig. S3*D*). For a pheromone diffusivity $\delta = 100\ \mu m^2/s$ and an intermediate degradation rate $\gamma = 1.0/h$, this gives an average prediction of a 1.74-mm floor thickness, in line with our observed measurements of 1.7 and 1.8 mm in MeMo80 and MeMo14, respectively. To evaluate model sensitivity, we also allow all parameters to vary across realistic ranges (*SI Appendix*, Table S2)—including three orders of magnitude for the degradation rate γ, as this value is the most variable in the literature (19). Across all parameter ranges, we observed floor thicknesses in the relatively constrained range 1.2 to 2.5 mm, with the greatest sensitivity to changes in the diffusivity δ and degradation rate γ as predicted by our scaling analysis (*SI Appendix*, Fig. S4).

Our simulated nests contained surface edges (topological defects, Fig. 3*C*) spanning across floors and sometimes forming traversable connections (Fig. 3*D*) corresponding to linear ramps—in which one floor terminates to provide the vertical space necessary for a simple ramp between adjacent floors—and helicoidal ramps, which wind about a vertical pillar that serves as a dislocation line spanning multiple floors (26) (*SI Appendix*, Fig. S5). By identifying the eventual location of a ramp, we observe the dynamical process by which ramps emerge from these defects during the construction process (Fig. 4*A*). Ramps first arise from regularly spaced floors in adjacent nest regions that are misaligned at the boundary via edge dislocation (in which an intermediate floor terminates at the boundary), which are connected to form a linear ramp to the floors above or below, or via screw dislocation (rotational misalignment about a slip plane), providing the axis of rotation about which a helicoidal ramp can be built (Fig. 3*C*). This misalignment of floor spacing is required for ramp formation; in follow-up simulations that initialized the mound with perfect floor regularity, ramps were altogether absent (*SI Appendix*). Moreover, when varying our model parameters, we find that two parameters control whether helicoidal ramps form at steady state: the scaled pheromone potency Hr_+/r_- and the scaled pheromone evaporation rate γ/r_-, yielding a phase space for their emergence (Fig. 4*B*). This is consistent with previous agent-based simulations of ant nest construction that pointed to the central role of the pheromone evaporation rate in influencing nest structures (19).

A fly-through of our simulated nests (Movie S2) reveals the structural similarity of the simulated nests produced by our model with the scanned *A. lamani* nests. To quantitatively evaluate this similarity, we gathered an identical set of statistics to describe the simulated nest topologies. We found that floor thickness and spacing between floors were similarly consistent in both the simulated and scanned nests, indicated by distributions with a similarly narrow variance (Fig. 4*C*). Moreover, the horizontal spacing between neighboring ramps on the same floor was

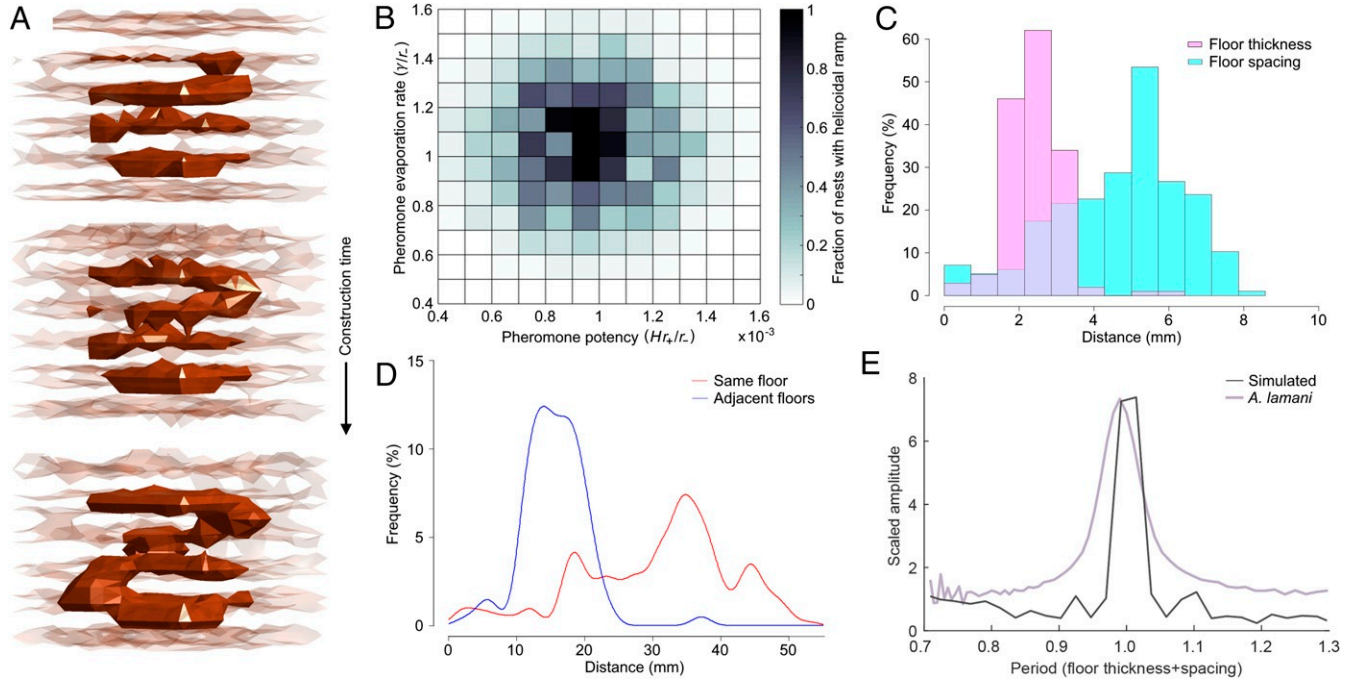

Fig. 4. Simulated nests resemble natural *A. lamani* nests and produce helicoidal ramps across a range of parameters. (*A*) Time snapshots of helicoidal ramp emergence during simulated nest construction, from early (*Top*) to late (*Bottom*) in the building period. (*B*) Heatplot for the frequency of helicoidal ramps in a simulated nest as a function of the two model parameters governing pheromone dynamics. (*C*) Histograms for floor thickness (pink) and spacing between floors (cyan), as measured in millimeters, averaged over simulated nests. The histograms show a pattern similar to the natural nests in Fig. 2*B*. (*D*) Density plot for the horizontal distance from a ramp to the nearest other ramp on the same floor (red) or on an adjacent floor above or below (blue), averaged over simulated nests and resembling the natural patterns shown in Fig. 2*C*. (*E*) The power spectrum of nest density, averaged over horizontal slices, peaks sharply at a one-floor period for both simulated (gray) and natural (purple) nests, indicating regularly spaced floor structures.

greater than the horizontal spacing between ramps on adjacent floors that often connected directly, as observed in the scanned nests (Fig. 4*D*). To assess the similarity of the simulated and scanned nests on large scales, we carried out a spectral analysis of the average nest density as a function of height for both the scanned and simulated nests and found that these density profiles are very similar (Fig. 4*E*). Together, these metrics indicate that the simulated nests resemble natural nests across global and local scales.

Emergent Biotectonics from Physics and Behavior

Our minimal theoretical framework links three spatiotemporal fields involved in the biotectonics of termite nests: dirt to constitute the nest, termite workers to shape the nest, and secreted pheromone to mark active regions of the nest. They allow us to capture two key geometrical and topological features of termite nests, namely the regular vertical spacing of floors and the horizontal spacing of ramps on the same or adjacent floors, as well as the months-long timing of the nest construction process (12). This feedback loop involving architecture, behavior, and information that drives nest construction is quite general in biological systems; relatedly, it is implicated also in the macromorphogenesis of termite mounds (18) and might provide insight into emergence of other animal architectures, such as ant nests or mounds and nests of other termite subfamilies (1, 19, 27). Understanding the complex ways in which these systems differ, while still adhering to the same fundamental principles, is a task for the future. Nevertheless, our finding that key termite nest structures emerge spontaneously in our model for a range of parameter values points to it being a nonequilibrium steady state that is robust and adaptable—a direct consequence of the ability of a colony to both lay down and respond to cues in its environment.

An important open question is the role of heat gradients and airflow within the nest (5, 6, 15), which are determined by the nest structure and in turn help to propagate pheromones and other signals, such as carbon dioxide levels (28). Although the diffusion rate of pheromones can range widely depending on their molecular weight and chemical properties, the pheromones we consider here have low diffusivities (20), and thus only provide a localized signal useful in nest construction. Given these low diffusivities, heat-driven airflow would result in a negligible change when incorporated into our model (*SI Appendix*, Fig. S6), although other potential odors with a higher diffusivity, such as those secreted by the queen, would be more susceptible to internal nest flow and hence more important to the larger-scale problem of the global templating and emergence of overall mound shape (18, 20). In the subterranean nests of *Apicotermes*, we expect that the role of heat gradients and airflow is minor relative to that in above-ground nests which are directly subjected to sunlight and air currents. Furthermore, because termite workers can move with relative ease through each nest, the initial dispersion pattern of workers within the nest would have minimal effect on the overall nest structure (*SI Appendix*, Fig. S7).

In constructing the functional, palatial structures of their nests, termites demonstrate a remarkable capacity for spontaneous self-organization through stigmergic interactions, coupling their behavior to deposited cues in their local environment—a process that stands in stark contrast to the planned building processes that give rise to human architecture. By studying the natural architectures that termites and other insects build and inhabit, and by understanding their ability to leverage their surroundings for information transfer, we can better understand how multiagent system approaches can be adapted for our own lives, from swarm intelligence to architectural design (29). After all, while we as humans have a mere ∼400,000 y of experience with

constructing primitive structures (30), mound-building termites of the family Termitidae have spent close to 50 million y (31) developing one of the grandest examples of architecture in the natural world.

Materials and Methods

X-Ray CT. Each nest was imaged using X-ray computed tomography with a medical scanner and reconstructed into a series of virtual cuts (512 × 512 pixels). MeMo13 and MeMo14 were scanned with a Somatom Sensation16 (Siemens) at Centre Hospitalier Universitaire (CHU) de Toulouse, Rangueil, France using exposure parameters of 120 kV and 150 mA, slice thickness of 1 mm, interslice distance 0.5 mm. MeMo80 was scanned with a LightSpeed Ultra (GE Medical Systems) at CHU Dijon using exposure parameters 100 kV and 170 mA, slice thickness of 0.625 mm, interslice distance 0.3 mm. Reconstruction of the virtual cuts (Fig. 1) was performed in the open-source software Horos (GNU Lesser General Public License, Version 3).

Investigation of Internal Structures. Ramps (with connecting holes to the floor above) and pillars (supporting the above floor without a passway) were identified by visual inspection of three orthogonal planes at each voxel of the original CT. For helices, identification was confirmed by reconstructing a perspective surface rendering (e.g., Fig. 1*C*). Mean coordinates for the base of each ramp or pillar were extracted (Fig. 2*A*) for the statistics in Fig. 2*C* and *SI Appendix*, Table S1. For Fig. 2*B*, MeMo14 was rotated to align horizontal floors with the *xy* plane with bilinear interpolation. The outer walls were removed from binarized images by first dilating each slice five times to close all outside openings and then defining an outline ROI of the nest, used to compute nest volume. All pixels outside the new ROIs were removed to obtain nests without outer walls as in Fig. 2*A*.

Floor thickness and floor spacing were measured by counting the number of consecutive black or white pixels in each vertical pixel line of the stacked images. The presence of pillars/ramps led to heavy right tails in both distributions, removed by cutting off all measures above twice the median floor height and alpha trimming the resulting distributions with $\alpha = 0.02$ on both sides. To check for the continuation of ramps across several floors, we selected for each floor the horizontal slice for which the horizontal pixel density was minimal (*SI Appendix*, Fig. S1*B*), computed the correlation coefficient between the pixels of adjacent floors, and compared them to the correlation coefficients between slices at least three floors separated (*SI Appendix*, Fig. S1*C*).

Numerical Solution of Model Equations. To simulate our construction model, we implemented a finite difference solver to numerically integrate the system of Eqs. **1**–**5**. We initialized each simulation with uniform nest density $u = 0.5$ (halfway packed) and uniform pheromone concentration $\rho = 0.1\,\mathrm{ng/cm^3}$, and with randomly scattered termite workers, such that the density of termites n at each grid location x was drawn from an exponential distribution with nondimensional mean 0.1. At each time step, the gradient and Laplacian of each of the three fields were calculated using second-order differencing in space, and the nest interior was then updated with first-order differencing in time. For each set of model parameters, 500 independent simulations were conducted.

Data Availability. The HTML three-dimensional images and Datasets S1 and S2 have been deposited in Harvard Dataverse (https://doi.org/10.7910/DVN/Z1GWTI) (32).

ACKNOWLEDGMENTS. We thank A. Robert for providing nest MeMo80 and the natural history museum in Paris for providing nests MeMo13 and MeMo14, both collected by P. P. Grassé. We are indebted to our reviewers for their careful reading and insightful suggestions. This work was supported by NSF Grant DGE-1144152 (to A.H.), Agence Nationale de la Recherche Grant ANR-06-BYOS-0008 (to G.T.), a China Scholarship Council PhD Grant (to L.G.), and the NSF Physics of Living Systems Grant PHY1606895 (to L.M.).

1. M. Hansell, *Animal Architecture* (Oxford University Press, 2005).
2. A. Perna, G. Theraulaz, When social behavior is molded in clay: On growth and form of social insect nests. *J. Exp. Biol.* **220**, 83–91 (2017).
3. C. C. Lee, K. B. Neoh, C. Y. Lee, Caste composition and mound size of the subterranean termite macrotermes gilvus (isoptera: Termitidae: Macrotermitinae). *Ann. Entomol. Soc. Am.* **105**, 427–433 (2012).
4. J. S. Turner, On the mound of macrotermes michaelseni as an organ of respiratory gas exchange. *Physiol. Biochem. Zool.* **74**, 798–822 (2001).
5. H. King, S. A. Ocko, L. Mahadevan, Termite mounds harness diurnal temperature oscillations for ventilation. *Proc. Natl. Acad. Sci. U.S.A.* **112**, 11589–11593 (2015).
6. S. A. Ocko *et al.*, Solar-powered ventilation of African termite mounds. *J. Exp. Biol.* **22**, 3260–3269 (2017).
7. S Camazine *et al.*, *Self-Organization in Biological Systems* (Princeton University Press, 2003), vol. 7.
8. D. J. T. Sumpter, *Collective Animal Behavior* (Princeton University Press, 2010).
9. C. Anderson, D. W. McShea, Intermediate-level parts in insect societies: Adaptive structures that ants build away from the nest. *Insectes Soc.* **48**, 291–301 (2001).
10. T. J. Czaczkes, C. Grüter, F. L. W. Ratnieks, Trail pheromones: An integrative view of their role in social insect colony organization. *Annu. Rev. Entomol.* **60**, 581–599 (2015).
11. E. Bonabeau, G. Theraulaz, J. L. Deneubourg, S. Aron, S. Camazine. Self-organization in social insects. *Trends Ecol. Evol.* **12**, 188–193 (1997).
12. J. Desneux, A. E. Emerson, *Les Constructions Hypogées des Apicotermes Termites de l'Afrique Tropicale* (Musée Royale du Congo Belge, 1952), vol. 17.
13. R. S. Schmidt, Functions of apicotermes nests. *Insectes Soc.* **7**, 357–368 (1960).
14. J. Korb, K. E. Linsenmair, The architecture of termite mounds: A result of a trade-off between thermoregulation and gas exchange?. *Behav. Ecol.* **10**, 312–316 (1999).
15. K. Singh *et al.*, The architectural design of smart ventilation and drainage systems in termite nests. *Sci. Adv.* **5**, eaat8520 (2019).
16. G. Theraulaz, E. Bonabeau, A brief history of stigmergy. *Artif. Life* **5**, 97–116 (1999).
17. P. P. Grassé, La reconstruction du nid et les coordinations interindividuelles chez-bellicositermes natalensis et cubitermes sp. la théorie de la stigmergie: Essai d'interprétation du comportement des termites constructeurs. *Insectes Soc.* **6**, 41–80 (1959).
18. S. A. Ocko, A. Heyde, L. Mahadevan, Morphogenesis of termite mounds. *Proc. Natl. Acad. Sci. U.S.A.* **116**, 3379–3384 (2019).
19. A. Khuong *et al.*, Stigmergic construction and topochemical information shape ant nest architecture. *Proc. Natl. Acad. Sci. U.S.A.* **113**, 1303–1308 (2016).
20. O. H. Bruinsma. "An analysis of building behavior of the termite macrotermes subhyalinus (Rambur)," PhD thesis Landbouwhogeschool Wageningen, Wageningen, The Netherlands, (1979).
21. M. A. Biot, General theory of three-dimensional consolidation. *J. Appl. Phys.* **12**, 155–164 (1941).
22. A. Stevens, The derivation of chemotaxis equations as limit dynamics of moderately interacting stochastic many-particle systems. *SIAM J. Appl. Math.* **61**, 183–212 (2000).
23. P. Amorim, Modeling ant foraging: A chemotaxis approach with pheromones and trail formation. *J. Theor. Biol.* **385**, 160–173 (2015).
24. R. S. Schmidt, Apticotermes nests. *Am. Zoologist* **4**, 221–225 (1964).
25. D. Fouquet, A. M. Costa-Leonardo, R. Fournier, S. Blanco, C. Jost, Coordination of construction behavior in the termite Procornitermes araujoi: Structure is a stronger stimulus than volatile marking. *Insectes Soc.* **61**, 253–264 (2014).
26. J. P. Hirth, J. Lothe, T. Mura, *Theory of Dislocations* (Cambridge University Press, 1983).
27. A. Perna *et al.*, Topological efficiency in three-dimensional gallery networks of termite nests. *Physica A* **387**, 6235–6244 (2008).
28. M. D. Cox, G. B. Blanchard, Gaseous templates in ant nests. *J. Theor. Biol.* **204**, 223–238 (2000).
29. J. S. Turner, R. C. Soar, "Beyond biomimicry: What termites can tell us about realizing the living building" in *Industrialised, Integrated, Intelligent sustainable Construction: I3CON Handbook 2*, I. Wallis, L. Bilan, M. Smith, A. S. Kazi, Eds. (I3CON & BSRIA Limited, Bracknell, UK, 2010), pp. 234–248.
30. P. Villa, *Terra Amata and the Middle Pleistocene Archeological Record of Southern France* (University of California Publications in Anthropology, Berkeley, CA, 1983), vol. 13.
31. D. A. Arab *et al.*, Parallel evolution of mound-building and grass-feeding in Australian nasute termites. *Biol. Lett.* **13**, 20160665 (2017).
32. A. Heyde, L. Guo, C. Jost, G. Theraulaz, L. Mahadevan, Termite biotectonics data. Harvard Dataverse. https://doi.org/10.7910/DVN/Z1GWTI. Deposited 12 November 2020.

PNAS
www.pnas.org

Supporting Information for

Self-organized biotectonics of termite nests

Alexander Heyde, Lijie Guo, Christian Jost, Guy Theraulaz, L. Mahadevan

Corresponding author: L. Mahadevan
Email: lmahadev@g.harvard.edu

This PDF file includes:

Supplementary Text
Figures S1 to S7
Tables S1 to S2
Legends for Movies S1 to S2
Captions for Datasets S1 to S2
SI References

Other supplementary materials for this manuscript include the following:

Movies S1 to S2
Datasets S1 to S2

Supplementary Text

Formulation of the continuum construction model

In formulating the dynamical equations (Eqs. 1-3) governing our model, we rely on the reaction-advection-diffusion framework (Britton 1986), in which the density of each quantity of interest (here we use the notation U for a general density) obeys a PDE of the form

$$\partial_t U = \nabla \cdot (K\nabla U - VU) + R(U), \tag{S1}$$

where $\nabla\cdot$ is the three-dimensional divergence operator and ∇ is the three-dimensional gradient operator, and where D denotes the diffusivity (as a matrix or scalar), V denotes the advection velocity (vector), and R denotes any non-spatial reaction dynamics (scalar function of U).

For the pheromone $U = \rho$, we assume a constant diffusivity $K = \delta$, no convection $V = 0$ (as we assume air flows are negligible within the subterranean nest), and two reaction terms: a production term proportional to the building rate f_+ (itself a function of ρ, see Eq. 4) and a standard exponential degradation term proportional to the pheromone density ρ, such that in total we have $R(\rho) = Hf_+(\rho) - \gamma\rho$.

For the termite workers $U = n_\pm$, where n_+ denotes the density of workers carrying dirt and n_- denotes the density of workers not carrying dirt, we assume a diffusivity that decreases with nest density u so that $K = D(1-u)$, convection as in chemotaxis that moves down the nest density gradient ∇u such that $V = -\chi\nabla u$ (with the negative sign indicating a bias towards low-density regions), and two reaction terms: $1/k$ termites converting from n_+ status to n_- status when building at rate f_+, and the reverse occurring when removing at rate f_-, so that in total $R(n_+) = (f_- - f_+)/k$ and $R(n_-) = -(f_- - f_+)/k$. Note that, overall, we model termites not carrying dirt as walking randomly (with a bias towards low-density nest regions) and searching for a dirt pellet to pick up, so that in local regions with high density, more dirt is available to be picked up, and therefore these are more likely sites for removal than regions with low density like tunnels and chambers. Termites trapped in high density regions may need to pick up dirt simply to excavate their surroundings and escape into a tunnel or chamber.

Finally, for the nest material $U = u$, we again assume no convection $V = 0$ and two reaction terms: building at rate $f_+(u)$ and removal at rate $f_-(u)$ – each also a function of u (see. Eqs. 4–5) so that in total $R(u) = f_+(u) - f_-(u)$. For the diffusivity matrix D, we set

$$D = \begin{pmatrix} 0 & 0 & 0 \\ 0 & 0 & 0 \\ 0 & 0 & g \end{pmatrix}, \tag{S2}$$

such that the nest material settles only in the direction of gravity, parallel to the z-axis. The effect of gravity can then be written more simply as $\nabla \cdot (D\nabla u) = \partial_z(g\partial_z u) = g\partial_z^2 u$, and this form is typical in the modeling of poroelastic materials (Biot 1941, Skotheim and Mahadevan 2004). For the poroelastic diffusivity scalar g, we use parameter values as indicated in Table S2 throughout; however, depending on the soil material and environmental conditions, we note that this may in fact vary from our estimate, although likely by no more than one order of magnitude.

Together, these assumptions are summarized as Eqs. 1-3 in the main text.

Non-dimensionalization of nest construction model

Although there are several parameters (Table S2) in our model of nest construction (see Eqs. 1-5 from the main text), our model takes an even simpler form when expressed in terms of just five non-dimensional parameters. To show this, first we rewrite Eqs. 1-4 in terms of the normalized variables $T = r_- t$, $\boldsymbol{X} = \boldsymbol{x}/L$, $\widetilde{\nabla} = \ell\nabla$ and $P = \rho r_+/r_-$ for time, position, height, and pheromone concentration respectively, where $\ell = (r/D)^{1/2}$ is the length scale for normalization. This gives

$$\text{Nest material density:} \quad \partial_T u = \partial_Z \left[\frac{g}{D}\partial_Z u\right] + f_+ - f_-, \tag{S3}$$

$$\text{Termite worker density:} \quad \partial_T n_\pm = \widetilde{\nabla}\cdot\left[(1-u)\widetilde{\nabla} n_\pm + \frac{\chi}{D} n \nabla u\right] \pm (f_- - f_+)k^{-1}, \tag{S4}$$

$$\text{Pheromone concentration:} \quad \partial_T P = \widetilde{\nabla}\cdot\left[\frac{\delta}{D}\widetilde{\nabla} P\right] + \frac{Hr_+}{r_-} f_+ - \frac{\gamma}{r_-} P, \tag{S5}$$

with $f_+ = n_+ P u(1-u)$ and $f_- = n_- u$. This non-dimensional system contains fewer parameters in the form of five dimensionless ratios. Specifically, these are the scaled pheromone potency Hr_+/r_-, the scaled evaporative flux γ/r, the pellet size k, and the scaled diffusivities δ/D, χ/D, and g/D that control the range of possible outputs from our model.

Floor scaling in nest construction model

In studying the behavior of our spatiotemporal model, we primarily use numerical simulations to assess the formation and arrangement of nest structures. However, the relative simplicity and symmetry in the mathematical formulation of our model allows for the derivation of a simple scaling prediction regarding the regularity of floor thickness.

At steady state, the building and removal rates must be balanced:

$$f_+ - f_- = r_+ n_+ \rho u(1-u) - r_- n_- u = 0. \tag{S6}$$

In terms of the steady state ratio $\eta = n_-/n_+$ of termite workers without dirt, this balance leads to either a no-density tunnel or chamber ($u = 0$) or a high-density floor or wall with density value

$$u^* = 1 - \frac{\eta r_-}{\rho r_+}. \tag{S7}$$

The stability condition $\partial_u(f_+ - f_-) < 0$ gives that tunnels ($u = 0$) occur at low pheromone levels ($\rho < \eta r_-/r_+$); here there is no building ($f_+ = 0$) nor removal ($f_- = 0$), and so the pheromone profile converges to $\rho = 0$. In contrast, structures ($u = u^*$) occur when the pheromone level is high ($\rho > \eta r_-/r_+$), and in the vicinity of a structure, the building and removal rates are both equal to the positive value $f_+ = f_- = r_- n_+ \eta u^*$.

It follows that, along the vertical (z) nest axis (in the direction of gravity, orthogonal to the floors), the steady-state pheromone profile $\rho(z)$ approximately satisfies a simplified form of Eq. 3 (or, equivalently, its dimensionless analog Eq. S5),

$$\delta\partial_z^2\rho + H\eta r_- \left(1 - \frac{\eta r_-}{\rho r_+}\right) - \gamma\rho = 0. \tag{S8}$$

There exists a flat profile $\rho(z) = \rho^* > 0$ stable to uniform perturbations if and only if the condition $\alpha = 1 - 4\gamma/Hr_+ > 0$ is met, which we derive by removing the first term of Eq. S8 and requiring

that the partial derivative with respect to ρ at steady-state be negative. After linearizing the above equation about $\rho = \rho^*$, we obtain the linear equation

$$\delta \partial_z^2 \rho + \frac{1}{2} Hr_+ (\rho - \rho^*)\left[\alpha - \sqrt{\alpha}\right] = 0. \tag{S9}$$

Looking for exponential solutions of the form $e^{\lambda z}$ we calculate the characteristic eigenvalues,

$$\lambda = \pm\sqrt{\frac{Hr_+}{2\delta}\left(\alpha - \sqrt{\alpha}\right)} = \pm\sqrt{\frac{2\gamma}{\delta}\,\frac{\alpha-\sqrt{\alpha}}{1-\alpha}}\,, \tag{S10}$$

which are complex conjugates because $Hr_+/\gamma > 0$, so $\alpha < 1$. Denoting the thickness of the floor structure by L, the relevant boundary conditions are that the pheromone vanish in the tunnels or chambers above and below the floor, represented by Dirichlet boundary conditions $\rho(-L/2) = \rho(L/2) = 0$. The thickness L then scales as one-half of the associated period, and so we have

$$L \sim \left[\frac{Hr_+}{\delta}\left(\sqrt{\alpha} - \alpha\right)\right]^{-\frac{1}{2}} = \left[\frac{4\gamma}{\delta} - \frac{Hr_+}{\delta}\left(1 - \sqrt{\alpha}\right)\right]^{-\frac{1}{2}}, \tag{S11}$$

where $0 < \alpha < 1$. This result implies that in the regime $\alpha \approx 1$ the floor thickness scales as $L \sim \sqrt{\delta/\gamma}$, the prediction that would arise in the case where floors are fully packed, $u^* \approx 1$. This regime is characterized by slow pheromone evaporation relative to its high deposition rate and potency. For our parameter values (Table S2), this prediction is a realistic 1.74 mm, consistent with our observations in MeMo80 and MeMo14. For the alternative extremal case $\alpha \approx 1$, in which the pheromone evaporation is sufficiently high to result in more diffuse nest interiors, the scaling law is plotted in Fig. S3D and is consistent with our full numerical simulations. We show sensitivity plots for how this floor thickness L varies with each parameter in Fig. S4.

Model of heat-driven air flow

The internal structures of termite nests not only determine the traversal patterns of workers; they also mediate the flow of air currents with the nest and thereby assist in ventilation and cooling (Turner 2001; King et al. 2015; Ocko et al. 2017). Although *A. lamani* nests are typically 30-50 cm below ground and are unlikely to be significantly influenced by conductive or wind-driven air flow, nest construction in other termite or social insect species may rely on air flow to propagate local information across longer scales. Previous models of termite mound ventilation and cooling have already been studied (Ocko et al. 2019; Singh et al. 2019)—yet it remains feasible that, in the nests of some species, these air currents may influence pheromone diffusion. As a result, we investigated the extent to which our modeling assumption of isotropic pheromone diffusion well approximates pheromone transport in a more complex model with advection by currents that flow preferentially along preexisting tunnels in the nest.

Due to the relatively low diffusivity δ of these building pheromones (Table S2), ensuring that the pheromone marks only a local region of the nest after deposition, we hypothesized that air currents should play a minimal role in influencing pheromone transport in our model. To numerically validate this, we simulated our model with the addition of air currents and the thermal fluctuations that drive them, as formulated in our prior work (Ocko et al. 2019). Using

this elaborated model, we then repeated our analysis of the simulated nest structures that formed. We found that helical ramps still emerged with the same structure and frequencies (Fig. S6A); that the pattern of regular spacing between floors (Fig. S6B) and ramps (Fig. S6C) remained qualitatively similar; and that the spectral analysis of nest density was minimally perturbed (Fig. S6D). Overall, we conclude that at the local scale of nest construction, the global effects of air currents on local pheromones are relatively inconsequential for the formation and arrangement of internal nest structures.

Nonetheless, air currents and the heat fluctuations that drive them are likely to play a central role in mediating the transport of other odors or pheromones that serve to provide a more global signal than the pheromones we consider in our analysis. These odors, such as the proposed "queen pheromone" secreted by the queen, could diffuse over much longer length scales in the mound as a means to infer distance from the nest (Grassé 1959). During construction of the mound as a whole, then, rather than only the nest topologies as considered here, these long-range odors are likely to be carried by air currents and to help define overall mound size and shape (Ocko et al. 2019).

Variations on the initial conditions

Although our analysis of our model was based on the generic assumptions described in the main text, we further considered two alternative but complimentary model variants to more thoroughly understand the structural dynamics of the simulated nests.

First, instead of initializing the model domain with a uniform soil density, characteristic of the environment surrounding a small nest poised for expansion, in a separate 100 simulations we alternatively initialized the model domain with preset, regularly spaced floors according to the initial density oscillation function

$$u = \frac{1}{2}\left(1 + \sin\frac{z}{4\pi L}\right), \tag{S12}$$

which oscillates with a period set at twice the floor thickness L, described above. In this subset of simulations, the initial presence of perfectly regular floor structure prohibited the emergence of any ramps; in total, across all simulations, not even one linear nor helicoidal ramp is detected, as stated in the main text.

Second, we tested another variant on our initial conditions in which the initial soil density was once again uniform as before, but the initial termite worker density was no longer randomly dispersed but instead concentrated at a central location according to the mean density function

$$n = A \exp\left[-\left(\frac{R}{L}\right)^2\right], \tag{S13}$$

where R denotes the Euclidean distance to the initial nest center and A is an amplitude chosen such that the total biomass of termites is maintained at the same level as previously. In these simulations, due to the relatively high dispersal rate of termites (we use 0.10-0.18 m^2/day), we find that the termites quickly disperse throughout the soil early in the building process, and so we obtain simulated nests that have nearly identical power spectra to those we obtained previously (Fig. S7).

Hypothesis testing for ramp spacing

To evaluate whether the distribution of ramps within nest floors was deliberate or random, we conducted a standard non-parametric hypothesis test (Kolmogorov-Smirnov) to determine if the spacing between a ramp and its nearest neighbor deviated significantly in either one of our two scanned nests from the expectations of a null model in which ramps are dispersed uniformly at random in the floor area.

We simulated 10,000 such nests under this null model and compared each to the data. We found that nearest ramps on the same floor were more distant across both of our scanned nests (p = 0.022 for MeMo14, p = 0.047 for MeMo80) than would be statistically expected by random chance, while nearest ramps on adjacent floors (either above or below) were closer (p = 0.040 for MeMo14, p = 0.046 for MeMo80) than statistically expected by chance, allowing for more efficient travel across vertical distances.

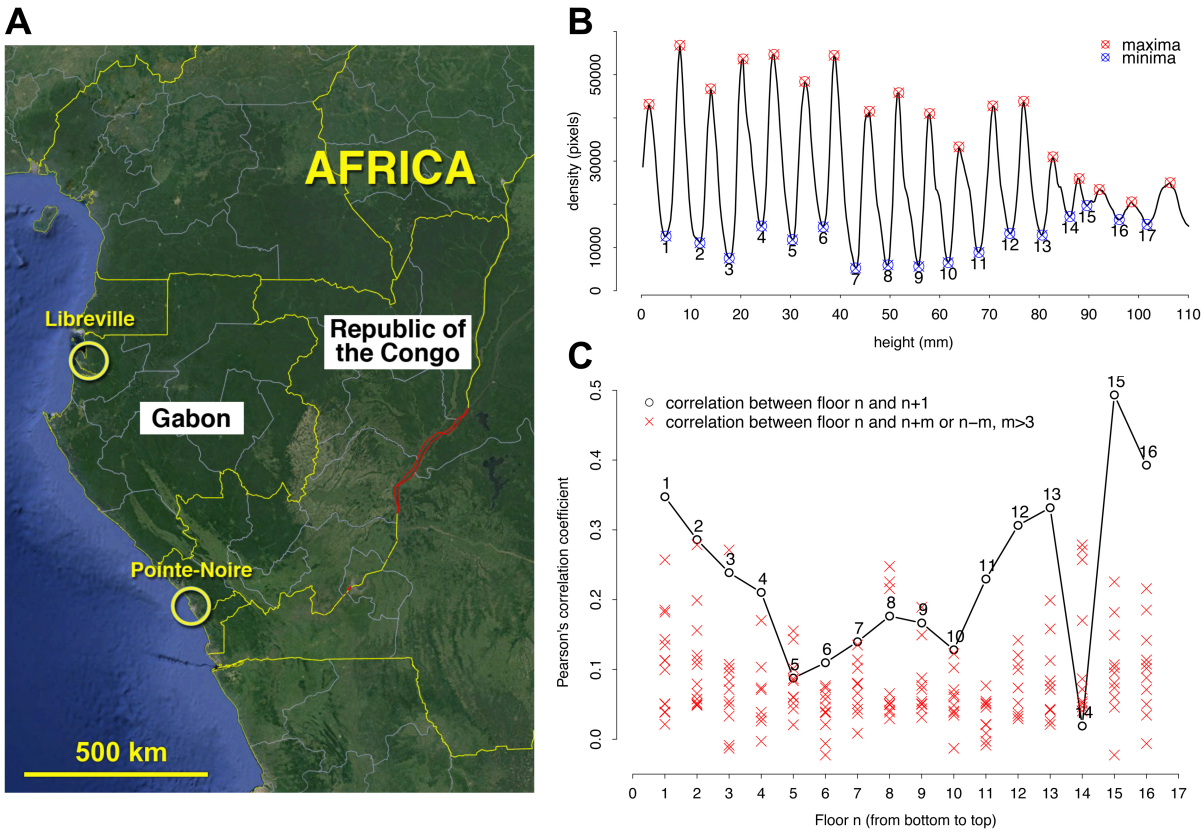

Fig. S1. Adjacent floors of *A. lamani* nests exhibit maximal similarity. (**A**) Sampling locations: two nests (MeMo14 and MeMo13) were collected near Libreville, Gabon; a third nest (MeMo80) was collected near Pointe Noire in Republic of the Congo. (**B**) Horizontal nest density (number of pixels) of MeMo80 (Fig. 2A) as a function of nest height shows a regular periodic signal. Maxima represent floors, while minima represent open space. Numbering corresponds to the floors in panel C and Fig. 2A-B. (**C**) Correlation between binary images of horizontal floor slices. Black circles represent Pearson's correlation coefficient between the pixel values of each floor n and that of the adjacent floor $n+1$ above it. Red crosses depict Pearson's correlation coefficient between the pixel values of each floor n and that of another floor at least 4 layers away. Across nearly all floors, adjacent floors had more similar densities than more distant floors. Above floor 13 the floors became convex (Fig. 2A, seen also in the horizontal density plot A as decreased amplitudes between minima and maxima), the slices therefore not only included pillars and ramps but also parts of the floors, degrading the correlation.

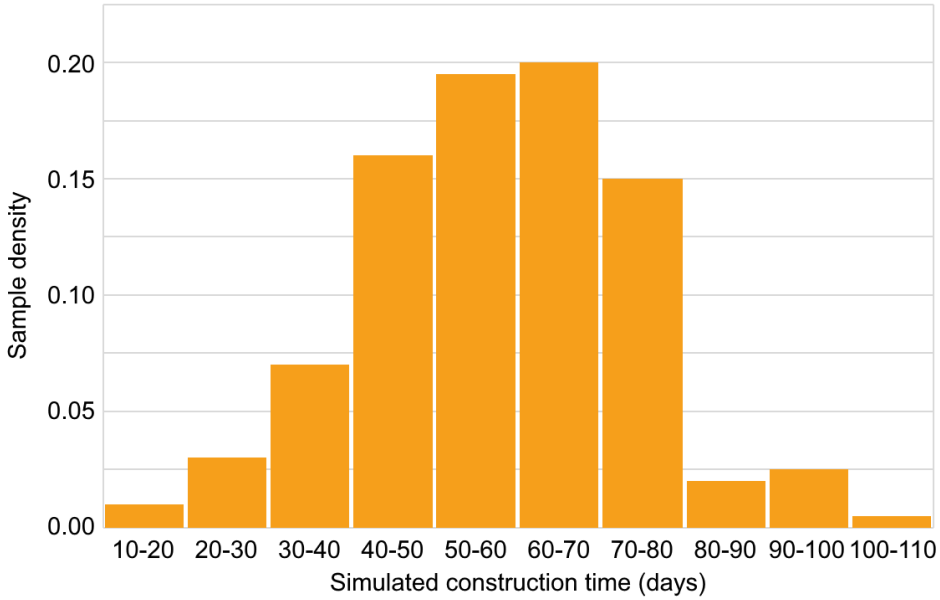

Fig. S2. Histogram of construction time for simulated termite nests. Across our base set of 500 simulated termite nests, using the parameter values in Table S2, simulations ranged in length from 11.3 days to 104.6 days, with a mean time of

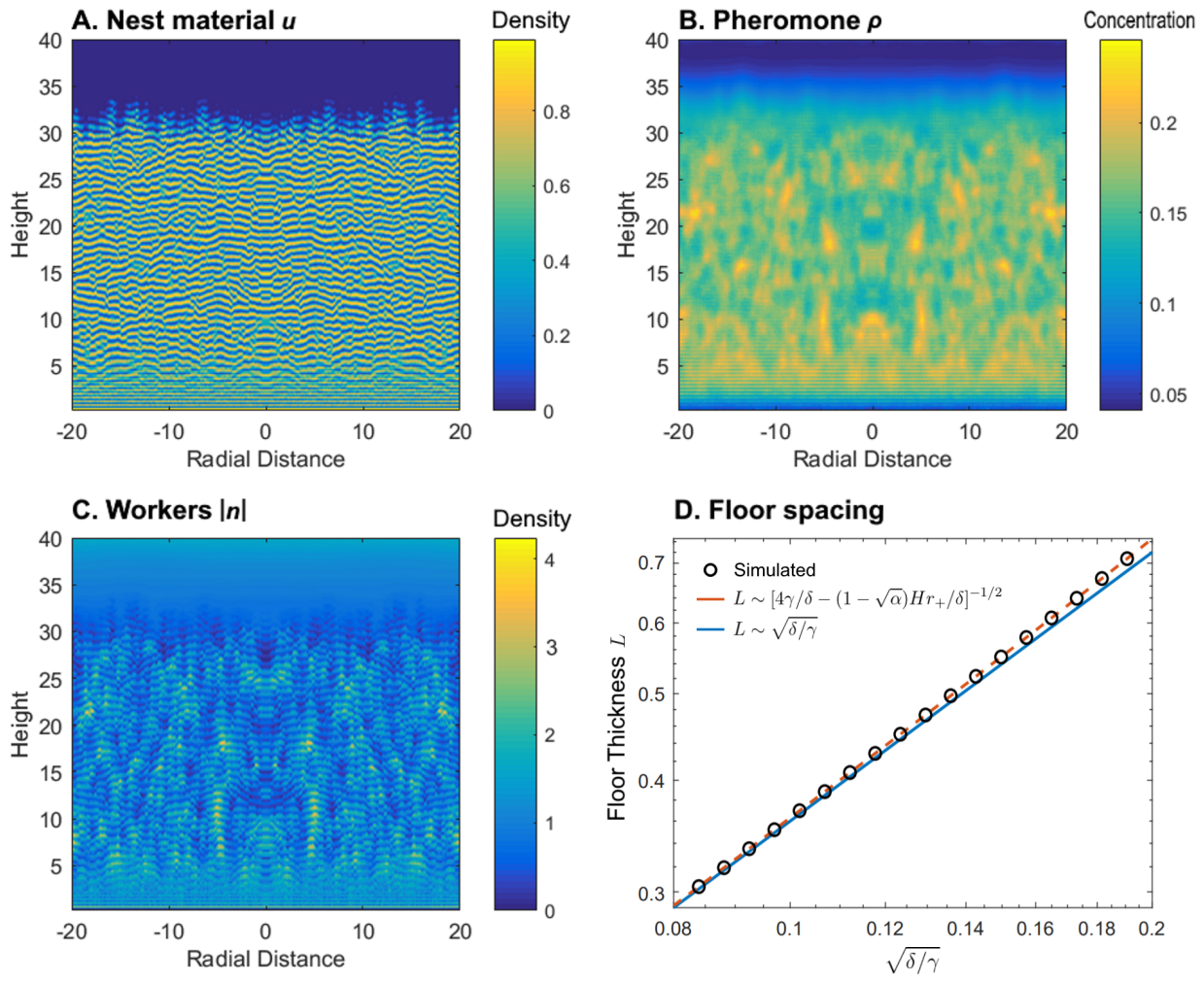

Fig. S3. Vertical slices and scaling from the spatiotemporal model. Model simulation results, with parameters set to their average values as listed in Table S2, are plotted as a vertical slice of each field through the central nest axis, colored by density or concentration according to the colorbar in each panel. (**A**) Vertical slice of nest material showing the regularity of floor spacing and dislocation. (**B**) Pheromone concentration in the same nest slice, showing that regions under active remodeling have a higher local pheromone concentration. (**C**) Worker density in the same nest slice, showing that regions under active remodeling also have a high density of termite workers. (**D**) Across all simulated nests, the steady-state floor thickness L (black circles) closely adheres to the scaling law given by Eq. S11 (orange dashed line), and approximately adheres to the simpler scaling law $L \sim (\delta/\gamma)^{1/2}$ (blue solid line).

A

	Parameter	Typical Values
δ	Diffusivity of pheromone	90–120 μm²/s
γ	Degradation rate of pheromone	0.01–10/hour
r_+	Nest building rate	30–80/hour/ng
H	Production rate of pheromone	1–10 ng/cm³

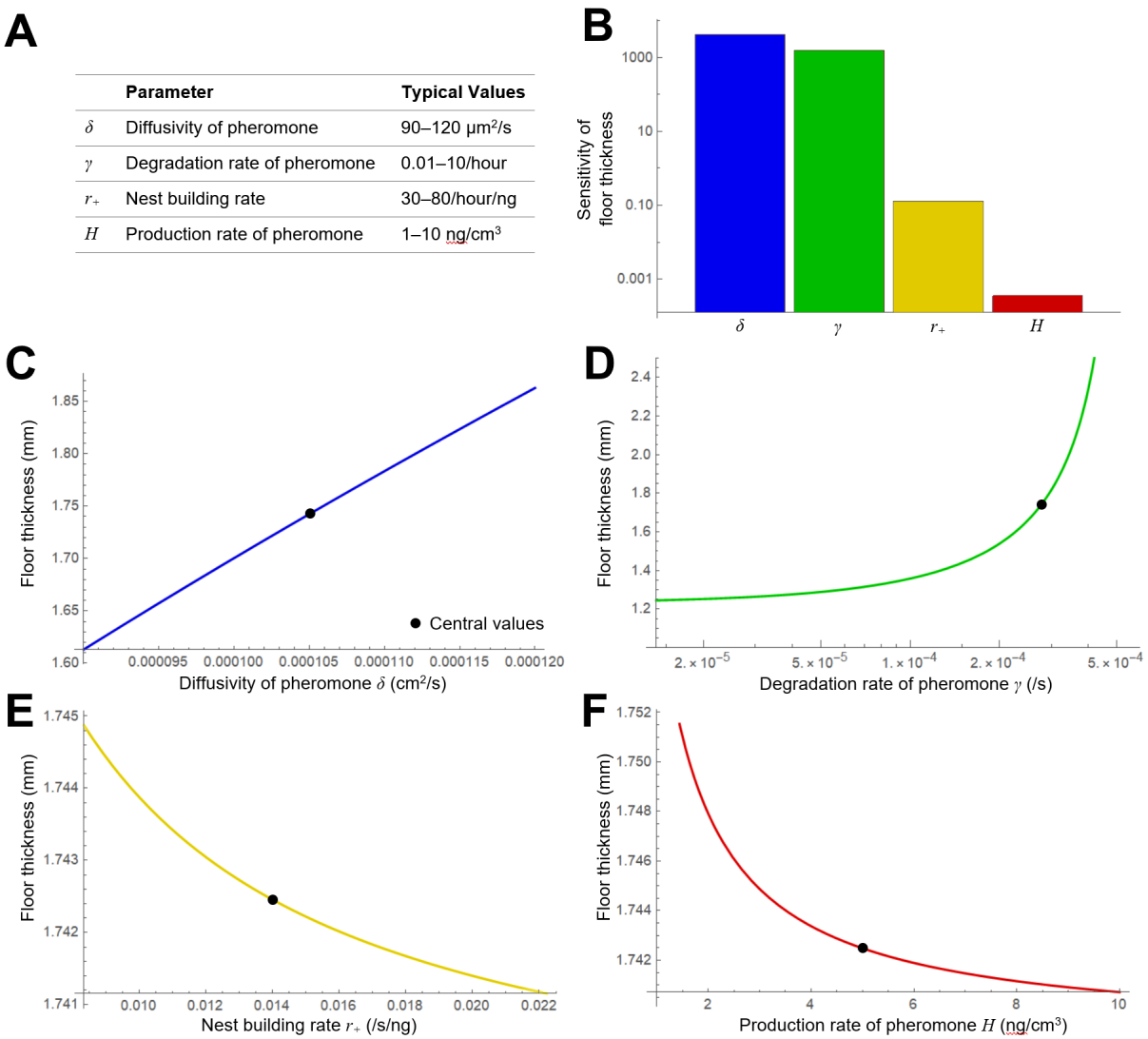

Fig. S4. Sensitivity analysis for floor spacing in the spatiotemporal model. The vertical spacing L between nest floors is determined by four model parameters with varying degrees of sensitivity. (**A**) Abbreviated table of the four model parameters that influence floor spacing (see Table S2 for a complete list of model parameters and typical values). (**B**) Sensitivity of our floor spacing law to each of these four model parameters, calculated as the magnitude of the partial derivatives. The floor thickness is most sensitive to the pheromone diffusivity and degradation rate. (**C-F**) Floor thickness L as a function of each parameter, holding all other parameters constant. Black dots indicate typical parameter values as used in panel B.

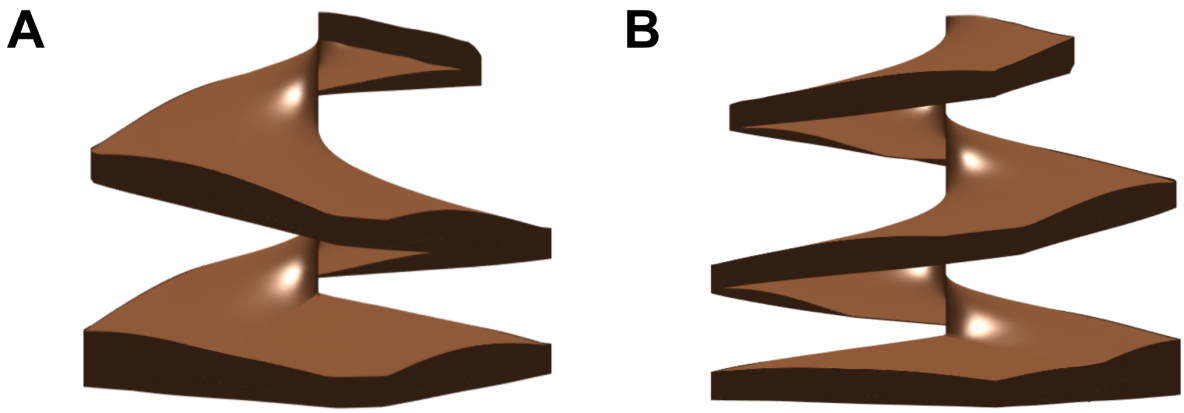

Fig. S5. Smoothed helicoidal ramps extracted from model simulation. Two exemplary helicoidal ramps with opposite chirality—(**A**) left-handed and (**B**) right-handed—were extracted from numerically simulated nest density fields and smoothed through a Gaussian filter with width equal to 0.2 of a floor thickness, in order to highlight the regularity of the helicoid. Model parameters were set to their average values from Table S2.

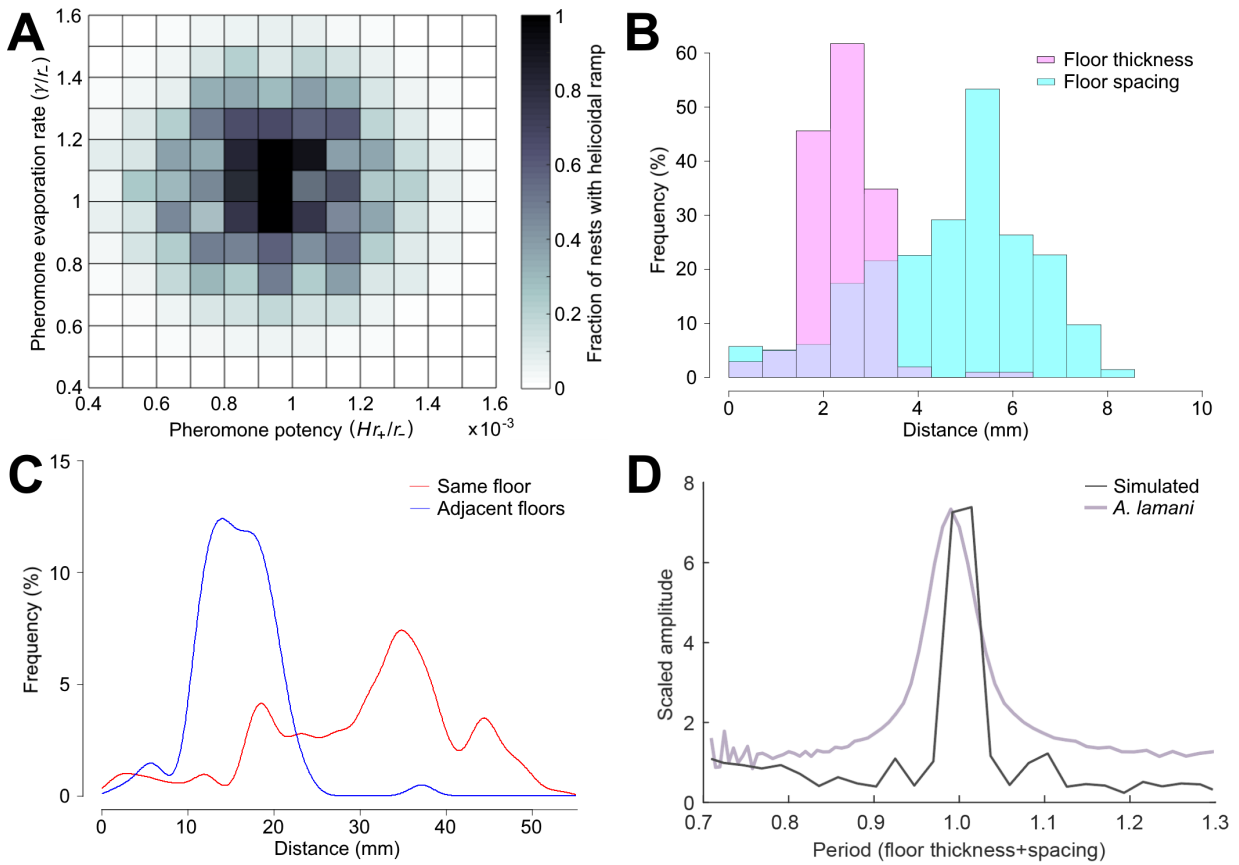

Fig. S6. Local nest structure is largely unchanged in response to heat-driven air flow. Incorporating heat and air flow into our spatiotemoporal model of nest morphogenesis results in negligible change to the structural statistics of our simulated nests (*cf.* Fig. 4), due to the low diffusivity of the building pheromone. (**A**) Heatplot for the frequency of helicoidal ramps in a simulated nest as a function of the two model parameters governing pheromone dynamics. (**B**) Histograms for floor thickness (pink) and spacing between floors (cyan), as measured in mm, averaged over simulated nests. The histograms show a pattern similar to the natural nests in Fig. 2c-d. (**C**) Density plot for the horizontal distance from a ramp to the nearest other ramp on the same floor (red) or on an adjacent floor above or below (blue), averaged over simulated nests and resembling the natural patterns shown in Fig. 2e-f. (**D**) The power spectrum of nest density, averaged over horizontal slices and transformed along the vertical axis, peaks sharply at the expected period (one floor thickness plus one floor spacing) for both simulated (gray) and natural (purple) nests, indicating regularly spaced floor structures.

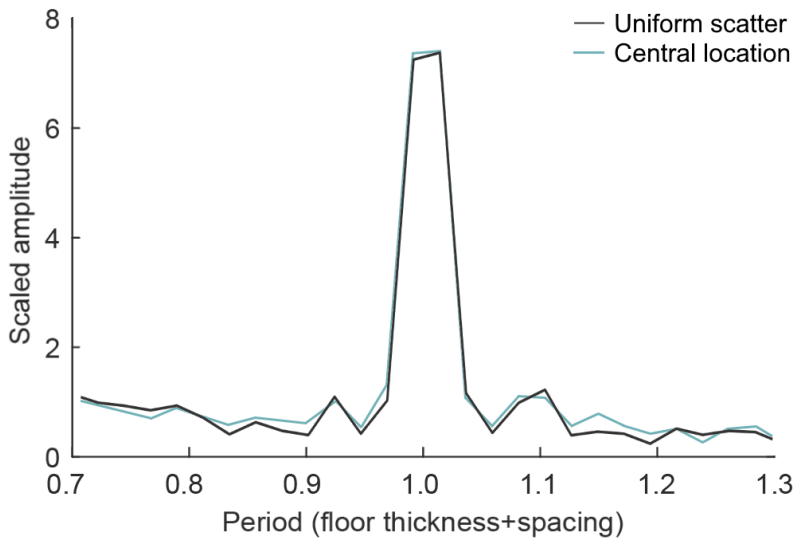

Fig. S7. Nest density power spectrum is minimally changed when termites are initially located at the nest center. To evaluate the sensitivity of the global structure of our nests to the initial dispersal pattern of termite workers within the soil, we ran an independent batch of simulations in which the termite workers were initially placed near to a single central location, rather than uniformly scattered throughout the soil. The power spectrum obtained from these new simulations (blue) closely resemble the spectra from our previous simulations (gray), indicating a similar overall nest structure.

Statistic	MeMo14	MeMo80
Nest height (cm)	25.2	13.8
Nest Volume (cm^3)	3084	1247
Number of floors analyzed	18	17
Number of linear ramps	23	15
Floors connected by linear ramps (median, min, max)	5, 2, 18	3, 2, 11
Volumetric density of linear ramps ($/m^3$)	7458	12029
Number of helices (chiralities)	0	5 (3 left, 2 right)
Floors connected by helices (median, min, max)	-	5, 4, 8
Volumetric density of helices ($/m^3$)	0	4010

Table S1. Statistics for *A. lamani* nests. Summary description of the analyzed nests MeMo14 and MeMo80. The number of floors analyzed refers to ramp and pillar detection.

Symbol	Description	Typical values
g	Poroelastic diffusivity of dirt	$4–8\times10^{-9}$ m^2/s (Bedayat 2014)
D	Maximal diffusivity of termites	0.10–0.18 m^2/day (Kareiva 1983)
χ	Chemotactic coefficient of termites	5–9 m^2/day (calculated from Amorim 2015)
k	Dirt pellet size	0.45–1.8 mg (Martius and Ribeiro 2010), 0.17–0.70 mm^3 (calculated for 2.6 mg/mm^3), 0.11–0.46 (scaled for dimensionless density u)
δ	Diffusivity of pheromone	90–120 $\mu m^2/s$ (Kaissling 2014)
H	Production rate of pheromone	1–10 ng/cm^3 (Sillam-Dussès et al. 2007)
γ	Degradation rate of pheromone	0.01–10/hour (Khuong et al. 2016)
r_+	Nest building rate	30–80/hour/ng (calculated from Khuong et al. 2016 and Sillam-Dussès et al. 2007)
r_-	Nest removal rate	10–30/hour (calc. from Khuong et al. 2016)

Table S2. Parameter symbols and typical values for spatiotemporal model. Our model integrates seven physical and biological parameters that jointly mediate the dynamics of nest construction and the structure of the final nest shape. Each parameter is represented by a symbol (left column) and a short description (middle column), and each has a range of typical values (right column) obtained and calculated from the listed references.

Our two movies can be downloaded from the PNAS site for this paper.

Movie S1. Video fly-through inside a scanned *A. lamani* nest MeMo80. This MP4 file was created using the open-source software Horos and can be viewed in a media player or web browser.

Movie S2. Video fly-through inside a simulated nest from our mathematical model. Model parameters were set to their average values as listed in Table S2. This MP4 file was created with MATLAB and can be viewed in a media player or web browser.

Our two datasets can be downloaded at the following public repository:
https://doi.org/10.7910/DVN/Z1GWTI

Dataset S1. Interactive 3D rendering of floor spacing and ramp placement in nest MeMo14. Orange planes indicate the mean floor positions within the nest. Color circles connected by line segments show the location of tunnels connecting adjacent floors, while grey cubes show the position of pillars on each floor. The black vertical line points to the top. This HTML file was created with the "rgl" package in R and can be viewed and rotated about its central black axis in a web browser.

Dataset S2. Interactive 3D rendering of floor spacing and ramp placement in nest MeMo80. Orange planes indicate the mean floor positions within the nest. Color circles connected by line segments show the location of tunnels connecting adjacent floors, while grey cubes show the position of pillars on each floor. The black vertical line points to the top. This HTML file was created with the "rgl" package in R and can be viewed and rotated about its central black axis in a web browser.

SI References

1. Britton, N. F. *Reaction-diffusion equations and their applications to biology*. Academic Press (1986).
2. Biot, M. A. General theory of three-dimensional consolidation. *Journal of Applied Physics*, *12*(2), 155-164 (1941).
3. Skotheim, J. M., & Mahadevan, L Dynamics of poroelastic filaments. Proc. R. Soc. Lond. A 460, 1995–2020 (2004).
4. JS Turner. On the mound of *Macrotermes michaelseni* as an organ of respiratory gas exchange. *Physiological and Biochemical Zoology*, 74(6):798–822, 2001.
5. H King, SA Ocko, and L Mahadevan. Termite mounds harness diurnal temperature oscillations for ventilation. *Proc. Natl. Acad. Sci. U.S.A.*, 112(37):11589–11593, 2015.
6. SA Ocko, H King, D Andreen, P Bardunias, JS Turner, R Soar, and L Mahadevan. Solarpowered ventilation of african termite mounds. *J Exper. Biol.*, 220(18):3260–3269, 2017.
7. SA Ocko, A Heyde, and L Mahadevan. Morphogenesis of termite mounds. *Proc. Natl. Acad. Sci. U.S.A.*, 116(9):3379–3384, 2019.
8. K Singh, BP Muljadi, AQ Raeini, C Jost, V Vandeginste, MJ Blunt, G Theraulaz, and P Degond. The architectural design of smart ventilation and drainage systems in termite nests. *Sci. Advances*, 5(3):eaat8520, 2019.
9. PP Grassé. La reconstruction du nid et les coordinations interindividuelles chezbellicositermes natalensis etcubitermes sp. la théorie de la stigmergie: Essai d'interprétation du comportement des termites constructeurs. *Insectes Sociaux*, 6(1):41–80, 1959.
10. Bedayat, H. *Poroelastic inhomogeneities: applications in reservoir geomechanics.* PhD thesis (Louisiana State University and Agricultural and Mechanical College, Louisiana, 2014).
11. Kareiva, P. M., & Shigesada, N. Analyzing insect movement as a correlated random walk. *Oecologia* (1983).
12. P Amorim. Modeling ant foraging: a chemotaxis approach with pheromones and trail formation. *Journal of Theoretical Biology*, 385:160–173, 2015.
13. Martius, C., & Ribeiro, J. D. Colony populations and biomass in nests of the Amazonian forest termite *Anoplotermes banksi* Emerson (Isoptera: Termitidae). *Studies on Neotropical Fauna and Environment,* 31(2): 82-86 (1996).
14. Kaissling, K. E. Pheromone reception in insects. *The example of silk moths in Neurobiology of Chemical Communication*, 99-146 (2014).
15. Sillam-Dussès, D., Sémon, E., Lacey, M. J., Robert, A., Lenz, M., & Bordereau, C. Trail-following pheromones in basal termites, with special reference to *Mastotermes darwiniensis*. *J. Chem. Ecol.*, 33(10), 1960-1977 (2007).
16. A Khuong, J Gautrais, A Perna, C Sbaï, M Combe, P Kuntz, C Jost, and G Theraulaz. Stigmergic construction and topochemical information shape ant nest architecture. *Proc. Natl. Acad. Sci. U.S.A.*, 113(5):1303–1308, 2016.